An integrated amorphous cobalt phosphoselenide electrocatalyst with high mass activity boosts alkaline overall water splitting

Yue Shi [a], Shuanglong Zhou [a], Jiaxin Liu [a], Xin Zhang [a], Jiao Yin [a], Tianrong Zhan [a], Yu Yang [a], Guangjiu Li [a], Jianping Lai [a, *], Lei Wang [a, b, **]

[a] State Key Laboratory Base of Eco-Chemical Engineering, International Science and Technology Cooperation Base of Eco-chemical Engineering and Green Manufacturing, College of Chemistry and Molecular Engineering, Qingdao University of Science and Technology, Qingdao 266042, PR China
[b] Shandong Engineering Research Center for Marine Environment Corrosion and Safety Protection, College of Environment and Safety Engineering, Qingdao University of Science and Technology, Qingdao 266042, PR China

ARTICLE INFO

ABSTRACT

Developing integrated non-noble metal electrocatalysts with mass activity comparable to noble metal is a significant challenge for overall water splitting. Herein, we constructed an integrated amorphous cobalt phosphoselenide (a-CoPSe) electrode via amorphization and dual anion-mediated strategy, achieving a significant improvement in the electrochemical active surface area (ECSA) and turnover frequency (TOF). The a-CoPSe offers large ECSA (65.9 $m^2 g^{-1}$) and high TOF values of 35.7 s^{-1} for hydrogen evolution reaction (HER) and 31.9 s^{-1} for oxygen evolution reaction (OER) at 300 mV. The mass activities of a-CoPSe are 890.4 A g_{Co}^{-1} for HER at 300 mV and 677.4 A g_{Co}^{-1} for OER at 250 mV, which are comparable to commercial Pt/C (10014.6 A g^{-1}) and RuO_2 (232.6 A g^{-1}). Theoretical calculation reveals amorphous cobalt with balanced charges regulated by phosphorus and selenium atoms simultaneously facilitate H_2O^*, H^*, OH^* and OOH^* adsorption, which greatly promotes the HER and OER kinetics.

1. Introduction

Water electrolysis is a promising technology for hydrogen production, in line with the concept of eco-friendly and carbon-neutral development [1–3]. Alkaline electrolyzer have attracted great attention because of their low operating costs, good durability and excellent capacity for hydrogen production [4–6]. Typical water splitting includes two half-reactions, hydrogen evolution reaction (HER) at the cathode and oxygen evolution reaction (OER) at the anode, which requires efficient electrocatalysts to accelerate the kinetics [7–10]. Traditionally, platinum and iridium/ruthenium oxides are state of the art candidates for catalyzing HER and OER, respectively [11–13]. However, their prohibitive cost is an unavoidable and insurmountable roadblock for practical application. Developing bifunctional catalysts could further simplify the equipment of alkaline electrolyzer and reduce operating expenses [12]. Therefore, exploring non-noble metal based catalysts to replace noble metal materials is always attempted for alkaline overall water splitting.

By far, extensive and ongoing efforts have focused on exploring advanced non-noble metal based catalysts alkaline water splitting [14–19]. Among them, cobalt based nanomaterials have been highlighted as promising candidates owing to their low cost, adjustable electronic structure and suitable absorption ability for reaction intermediates [20–23]. In particular, integrated electrocatalysts are binder-free and self-supported, which facilitates charge and mass transport, active site exposure and long-term operation [24–26]. Despite these considerable advancements, the mass activities of non-noble metal integrated catalysts remain inferior to noble metal catalysts. The limited mass activities are caused by insufficient electrochemical active surface area and poor intrinsic activity (inability to simultaneously optimize the adsorption of H_2O^*, H^*, OH^* and OOH^* intermediates).

Herein, we reported an integrated amorphous cobalt phosphoselenide (a-CoPSe) with flexible charge density to achieve a significant improvement in the mass activity of non-noble metal integrated catalysts. During the one-step electrodeposition method, the incorporation of phosphorus and selenium atoms with different electronegativity not

---

only contributes to forming disordered structures, but also allows to effectively regulate the electronic structure of the catalyst. The amorphous structure possesses more defects and surface dangling bonds available as active sites, which are more beneficial for catalysis. The a-CoPSe loaded on the nickel foam (NF) achieves outstanding catalytic activity for alkaline water splitting. It only requires the overpotentials of 285 and 244 mV to drive 500 mA cm^{-2} for HER and OER, far superior to commercial catalysts and most reported materials. The mass activities of a-CoPSe are up to 890.4 A g_{Co}^{-1} at the overpotential of 300 mV for HER and 677.4 A g_{Co}^{-1} at the overpotential of 250 mV for OER, comparable to commercial noble metal catalysts. Moreover, the self-supporting loose structure provides good mass transfer and ensures long-term stability. Density functional theory (DFT) calculations further demonstrate that a-CoPSe displays optimal Gibbs free energies of H$_2$O* , H* and OH* species adsorption during HER. Meanwhile, the amorphous Co sites with balanced charges regulated by phosphorus and selenium atoms greatly reduce the energy barriers of OH* and OOH* evolution, which contributes to promoting the OER kinetic. The operando Raman spectra further prove that incorporating phosphorus and selenium atoms accelerates the formation of CoOOH active species in the OER process.

2. Experimental section

2.1. Chemicals

Cobalt (II) dichloride hexahydrate (CoCl$_2$·6H$_2$O, Sigma-Aldrich, >98%), sodium hypophosphite (NaH$_2$PO$_2$, Aladdin, 95%), selenium dioxide (SeO$_2$, Macklin, >99%), ammonium chloride (NH$_4$Cl, Aladdin, 99.5%), potassium hydroxide (KOH, Aladdin, 90%). The deionized water used in all experiments was ultrapure water (18.2 MΩ·cm).

2.2. Materials synthesis

The integrated a-CoPSe was synthesized by the galvanostatic electrodeposition method at ambient temperature. In order to eliminate surface oxides and contamination, NF was ultrasonically treated for 10 min in acetone and 1.0 M HCl, respectively. The treated NF was cleaned with deionized water and used as the working electrode. Electrodeposition was carried out on a three-electrode system. The reference electrode and counter electrode were saturated calomel electrode (SCE) and graphite rod, respectively. The electrolyte was obtained by dissolving 0.1 M CoCl$_2$·6H$_2$O, 0.1 M NaH$_2$PO$_2$, 0.1 M SeO$_2$ and 0.12 M NH$_4$Cl in the deionized water. Subsequently, galvanostatic electrodeposition was performed under a current density of − 20 mA cm^{-2} for 10 min. After electrodeposition, the obtained a-CoPSe was distributed on the surface NF. Subsequently, the a-CoPSe electrode was cleaned with deionized water and dried in a drying oven. The c-CoP and c-CoSe were prepared by the same process, except for the contents of the electrolyte. For c-CoP, the electrolyte was composed of 0.1 M CoCl$_2$·6H$_2$O, 0.2 M NaH$_2$PO$_2$ and 0.12 M NH$_4$Cl. For c-CoSe, the electrolyte included 0.1 M CoCl$_2$·6H$_2$O, 0.2 M SeO$_2$ and 0.12 M NH$_4$Cl. In addition, c-CoP/CoSe was prepared by a two-step galvanostatic electrodeposition process. Firstly, NF was electrodeposited in the electrolyte of c-CoP for 5 min, and then transferred to the electrolyte of c-CoSe for another 5 min to obtain the c-CoP/CoSe electrode.

2.3. Characterization

Scanning electron microscopy (SEM) images were obtained by Hitachi, S-8200 (Japan). The transmission electron microscope (TEM) and high-resolution TEM (HRTEM) of the catalyst were tested using FEI Tecnai-G2 F30 at an accelerating voltage of 300 KV. Powder X-ray diffraction (XRD) patterns were recorded on an X'Pert-Pro MPD diffractometer with Cu Kα radiation at 40 KV and 40 mA. X-ray photoelectron spectroscopy (XPS) analysis was performed with an Axis Supra spectrometer using a monochromatic Al Kα source (15 mA, 14 kV). Scan

analysis with an analysis area of 300 × 700 μm and a pass energy of 100 eV. The XPS spectra were calibrated by carbon 1 s spectrum, and its main line was set to 284.6 eV. Raman spectra were collected on a confocal Raman microscope (Renishaw inVia) with an argon-ion laser (λ = 532 nm) in ambient air.

2.4. Electrochemical measurements

The electrochemical measurements were carried out on the CHI 760E Electrochemical Workstation (CH Instruments, Inc., Shanghai). The HER and OER performance of catalysts were evaluated by a typical three-electrode system in 1.0 M KOH solution. The working electrodes were self-supporting NF loaded with different nanomaterials. The reference electrode and counter electrode were SCE and graphite rod, respectively. The potentials were converted to the reversible hydrogen electrode (RHE) according to the Nernst equation: $E(RHE) = E(SCE) + 0.244V + 0.059 \times pH$. The typical polarization curves were obtained through linear sweep voltammetry (LSV) measurements with the scan rate of 5 mV s^{-1} and corrected for 95% iR compensation level. Electrochemical impedance spectroscopy was measured in the frequency range from 100 kHz to 0.1 Hz. The electrochemically active surface area (ECSA) was calculated by the electrochemical double-layer capacitance (C_{dl}) method. To derive the C_{dl}, the following equation was used: $C_{dl} = Ic/\nu$, where Ic is the charging current (mA cm^{-2}) and ν is the scan rate (mV s^{-1}). The ECSA was calculated according to the following equation: $ECSA = C_{dl} \times S/C_s \times m$, where S is the surface area of the electrode (cm^{-2}), Cs is the specific capacitance (0.040 mF cm^{-2}) and m is the mass loading of catalysts. The turnover frequency (TOF) values were calculated from the following equation: $TOF = j/k \times F \times n$. Here, k is the number of electron transfer (the factors of HER and OER are respectively 2 and 4), j is the current (A) during LSV with 95% iR-corrected, F is the Faraday constant (96485.3 C mol^{-1}), n is the number of active sites (mol). The number of voltammetric charges is gained by CV curves from − 0.2–0.6 V (vs. RHE) in phosphate buffer solution (pH = 7) with a scan rate of 50 mV s^{-1} and the following equation is $n = Q/2F$.

2.5. DFT computations

DFT calculations were performed with the VASP package [27,28]. Zero damping D3 correction method of Grimme was used to describe van der Waals interactions [29]. The generalized gradient approximation of Perdew-Burke-Ernzerhof was used to calculate exchange-correlation energies, where the force-, energy-convergence criterion for self-consistent field, and energy cutoff were set to 1×10^{-5} eV, 0.05 eV Å^{-1}, and 450 eV, respectively. A Gamma ($1 \times 1 \times 1$) k-point grid was employed for faster convergence during optimization [30,31]. Free energy diagrams for HER were computed using a computational hydrogen electrode model, which suggests that the chemical potential of a proton/electron is equal to half of that of one H$_2$ gas molecule [32]. The change in free energy (ΔG) for each step in the overall transformation was determined using the following equation, $\Delta G = \Delta E + \Delta ZPE - T\Delta S$, where ΔE, ΔZPE, and ΔS are the differences in the total energies, zero-point energies, and entropies between the reactant and product, respectively [33]. The zero-point energy values reported by Nørskov et al. were used for all reaction steps, and ΔS was taken from thermodynamic tables at T = 298 K.

3. Results and discussion

3.1. Synthesis and structural characterization

Due to its excellent electrical conductivity and structural stability, NF is considered as an ideal matrix required for the preparation of integrated catalysts (Figs. S1–2). Different from gaseous atmosphere and solvothermal reaction, electrodeposition method has the distinct advantage of realizing rapid preparation at ambient temperature and

pressure. We chose CoCl$_2$·6H$_2$O as the cobalt source, SeO$_2$ as the selenium source, and NaH$_2$PO$_2$ as the phosphorus source [34–36]. The NH$_4$Cl was used as a complexing agent [37]. In the corresponding reducing voltage, the H$_2$PO$_2^-$ and SeO$_3^{2-}$ will be reduced and interact with the Co^{2+} in solution to form CoP$_x$Se$_y$. After galvanostatic electrodeposition by a three-electrode system, the synthesized catalyst was anchored to the surface of NF (Fig. 1a). SEM image reveals that the prepared a-CoPSe uniformly loaded onto the surface of the NF like a loose nanoskin, which facilitates sufficient contact with reactants and mass transfer (Fig. 1b and S3). TEM image further indicates that a-CoPSe is formed by the interlinking of nanoplates (Fig. 1c). To analyze the atomic arrangement structure of a-CoPSe, HRTEM and selected area electron diffraction (SAED) technologies are utilized. Disordered lattice fringes in the HRTEM images and broad diffraction rings in the SAED pattern combine to accurately illustrate the amorphous structure of a-CoPSe (Fig. 1d-f). The formation of amorphous structures is probably due to the interference of phosphorus and selenium atoms completely breaking the orientation arrangement of cobalt atoms during the electrodeposition process. In addition, the high-angle annular dark-field scanning TEM (HAADF-STEM) and corresponding energy dispersive X-ray (EDX) elemental mapping images shown in Fig. 1g elucidate the homogenous distribution of Co, P and Se elements throughout the catalysts. The EDX line scan image further corroborates the above conclusion (Fig. S4). According to the EDX spectrum, the atomic ratio of Co/P/Se in nanoplates is about 52.9/40.4/6.7, in line with the data from inductively coupled plasma-atomic emission spectroscopy (Fig. S5 and Table S1). By adjusting the composition of the electrolyte, the crystalline

cobalt phosphide (c-CoP) and crystalline cobalt selenide (c-CoSe) were prepared by one-step electrodeposition. In Fig. S6, the c-CoP appears as nanosheets and grows uniformly on the NF substrate. The lattice fringe with interplanar spacing of 0.22 nm is consistent with the (222) lattice plane of CoP crystal (Fig. S7). Different from c-CoP, c-CoSe is loaded on the NF surface in the shape of nanoparticles (Fig. S8). The HRTEM image shows that the lattice spacing of 0.27 nm in nanoparticles matches the (101) lattice plane of the CoSe crystal (Fig. S9). The great difference between the morphology of c-CoP and c-CoSe may arise from two completely different nonmetallic atoms. In the presence of both nonmetallic atoms, the morphology of the prepared catalysts is between nanoparticles and nanosheets, showing the interconnected nanoplate structure described previously. For subsequent studies, crystalline cobalt phosphide and cobalt selenide heterostructure (c-CoP/CoSe) was also fabricated employing the electrodeposition strategy. SEM image shows that c-CoP/CoSe exhibits nanosheets and some nanoparticles tightly attached on the surface (Fig. S10). TEM image later confirms that the c-CoP/CoSe is a combined structure of nanosheets and nanoparticles (Fig. S11a). In Fig. S11b-e, distinct lattice fringe in the nanosheet and nanoparticle regions were selected for analysis, respectively. The blue frame is from the nanosheet fraction, and the corresponding lattice spacing is 0.22 nm aligned with the (222) lattice plane of the CoP crystal (Fig. S11b-c). The yellow frame is from the nanoparticle fraction, and the internal lattice spacing is 0.20 nm matching the (102) lattice plane of CoSe crystal (Fig. S7d-e). The HRTEM results demonstrate the successful synthesis of crystalline CoP/CoSe heterostructures. More importantly, it is evidenced that the competition between different
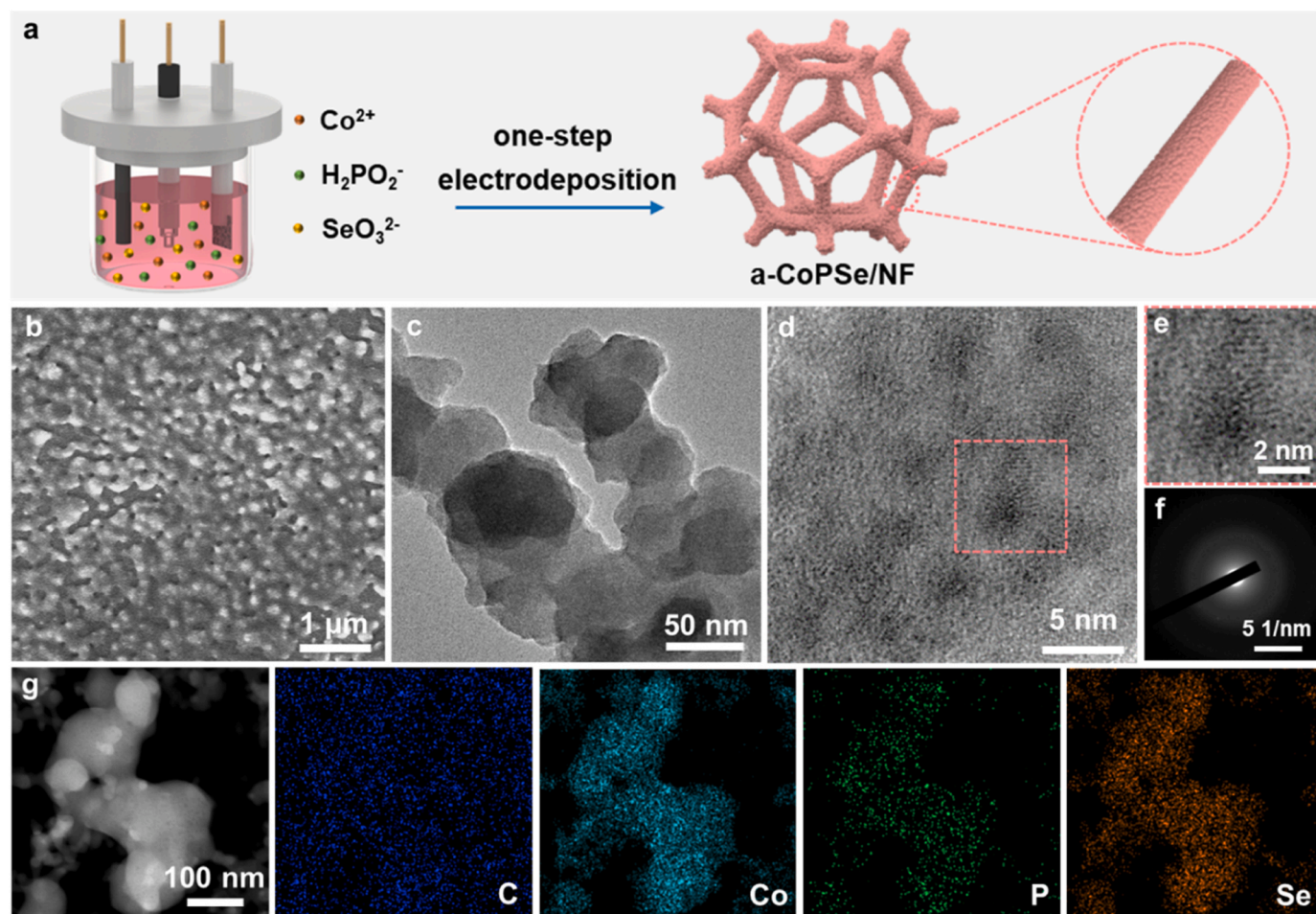

Fig. 1. Morphology and structure characterizations of a-CoPSe. (a) Schematic illustration of the formation process. (b) SEM image. (c) TEM image. (d-e) HRTEM image. (f) SAED pattern. (g) HAADF-STEM and corresponding EDX mapping images.

nonmetallic atoms causes the generation of amorphous structures during the electrodeposition.

The crystal structure of the above nanomaterials was further confirmed by XRD patterns. As shown in Fig. 2a, the diffraction peaks of c-CoP/CoSe match well with the standard cards of CoP (JCPDS No. 29–0496) and CoSe (JCPDS No. 52–1008), which are consistent with the corresponding HRTEM images. The peaks matched with Ni (JCPDS No. 04–0850) come from NF. By contrast, no obvious diffraction peak except NF could be observed in the XRD pattern of a-CoPSe, further proving the amorphous structure. Furthermore, the XRD patterns of c-CoP and c-CoSe were also detected (Fig. S12-13). In addition to the peaks of NF, the diffraction peaks of c-CoP are assigned to the standard cards of CoP (JCPDS No. 29–0496), and the diffraction peaks of c-CoSe are indexed to the standard cards of CoSe (JCPDS No. 52–1008). XPS was further applied to explore the chemical composition and electronic state of catalysts. The XPS survey spectra of c-CoP/CoSe and a-CoPSe demonstrate the presence of Co, P and Se atoms on the sample surface (Fig. S14). The oxygen species detected are probably caused by surface oxidation occurring in the atmosphere. The presence of carbon could be due to the use of conductive carbon materials during the XPS testing. In Fig. 2b, the high-resolution XPS spectrum of Co 2p for c-CoP has two dominant peaks at around 781.3 and 797.2 eV corresponding to Co^{2+} $2p_{3/2}$ and Co^{2+} $2p_{1/2}$, respectively [38–40]. Another two small and broad peaks located at 785.9 and 803.2 eV are shakeup satellites of Co^{2+} (denoted as sat.). After incorporating Se atoms, the binding energy of the Co^{2+} $2p_{3/2}$ peaks in c-CoP/CoSe and a-CoPSe indicate the positive shift

of 0.05 and 0.2 eV in comparison with c-CoP, revealing the Co sites are in an electron deficient state. The above phenomenon is attributed to the strong electronegativity of Se atoms, which could attract some electrons around Co atoms. Remarkably, the electron transfer is significantly stronger for a-CoPSe compared to c-CoP/CoSe, which is due to the favorable interaction between different atoms in an amorphous structure. As shown in Fig. 2c, the high resolution XPS spectrum of P 2p for a-CoPSe can be deconvoluted into three peaks assignable to P $2p_{3/2}$ (129.7 eV), P $2p_{1/2}$ (131.0 eV) and P-O (134.9 eV).[41–43] Moreover, the Se 3d spectrum for a-CoPSe displays two prominent peaks at around 54.6 and 55.5 eV, which are ascribed to Se $3d_{5/2}$ and Se $3d_{3/2}$ (Fig. 2d) [44]. In addition, an oxidation peak at around 59.2 eV is associated with SeO_x [45].

3.2. HER and OER performance evaluation

The electrochemical performances of catalysts were evaluated in alkaline electrolytes using a standard three-electrode cell. The obtained cobalt-based nanomaterials grown on NF directly acted as the working electrodes. Firstly, the HER properties of as-prepared electrodes were investigated in 1.0 M KOH. As the benchmark HER catalyst, commercial Pt/C (20 wt%) was also included for comparison. Fig. 3a presents the LSV curves of the samples after corrected for 95% iR compensation. Compared with other catalysts, the current density of a-CoPSe electrode grows rapidly with the increased overpotential, demonstrating outstanding HER activity. The a-CoPSe achieves large current densities
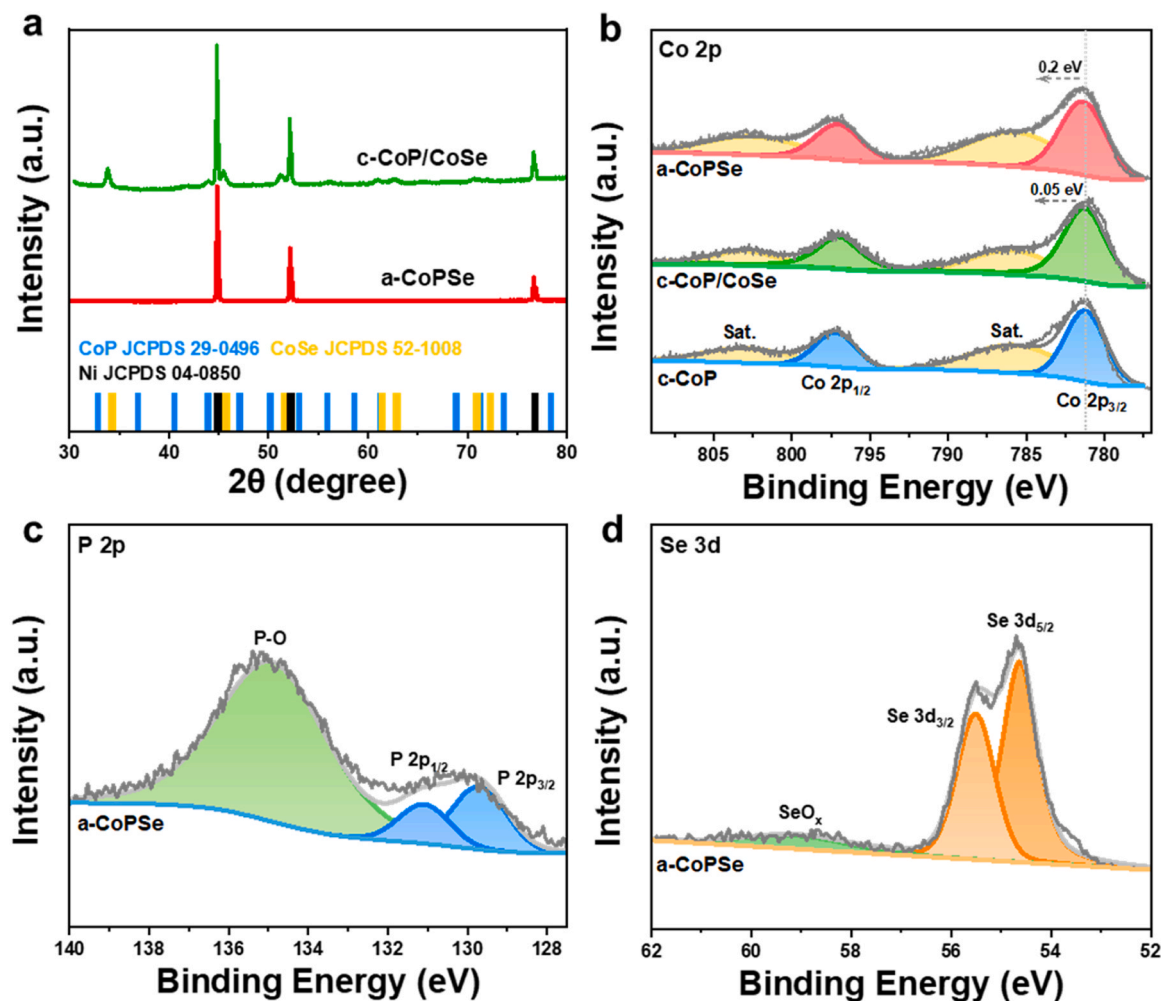

Fig. 2. Structure characterizations. (a) XRD patterns of a-CoPSe and c-CoP/CoSe. (b) High-resolution Co 2p XPS spectra of as-prepared catalysts. High-resolution (c) P 2p and (d) Se 3d XPS spectra of a-CoPSe.
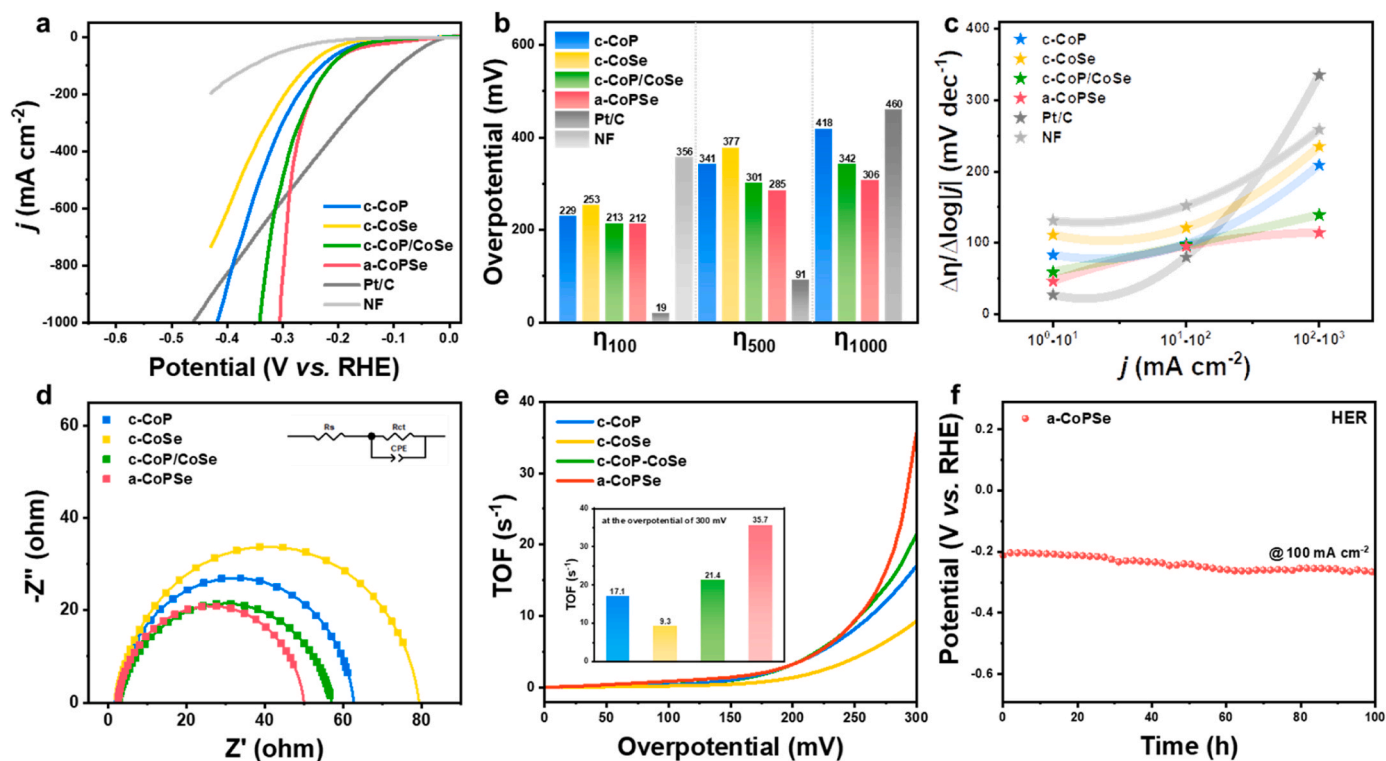
Fig. 3. HER performance in 1.0 M KOH. (a) Polarization curves. (b) The overpotentials at the current density of 100, 500 and 1000 mA cm^{-2}. (c) $\Delta\eta/\Delta\log|j|$ ratios at different current densities. (d) Nyquist plots. (e) TOF values. (f) Chronopotentiometry curve of a-CoPSe.

of 100, 500 and 1000 mA cm^{-2} at quite low overpotentials of 212, 285 and 306 mV, far superior to the prepared catalysts and commercial Pt/C (specific data are shown in Fig. 3b). The trends in Tafel slopes are critical

for performance evaluation under high current densities [46,47]. The Tafel slopes ($\Delta\eta/\Delta\log|j|$) of all samples under different current densities were counted (Fig. 3c). The slower the $\Delta\eta/\Delta\log|j|$ grows with current
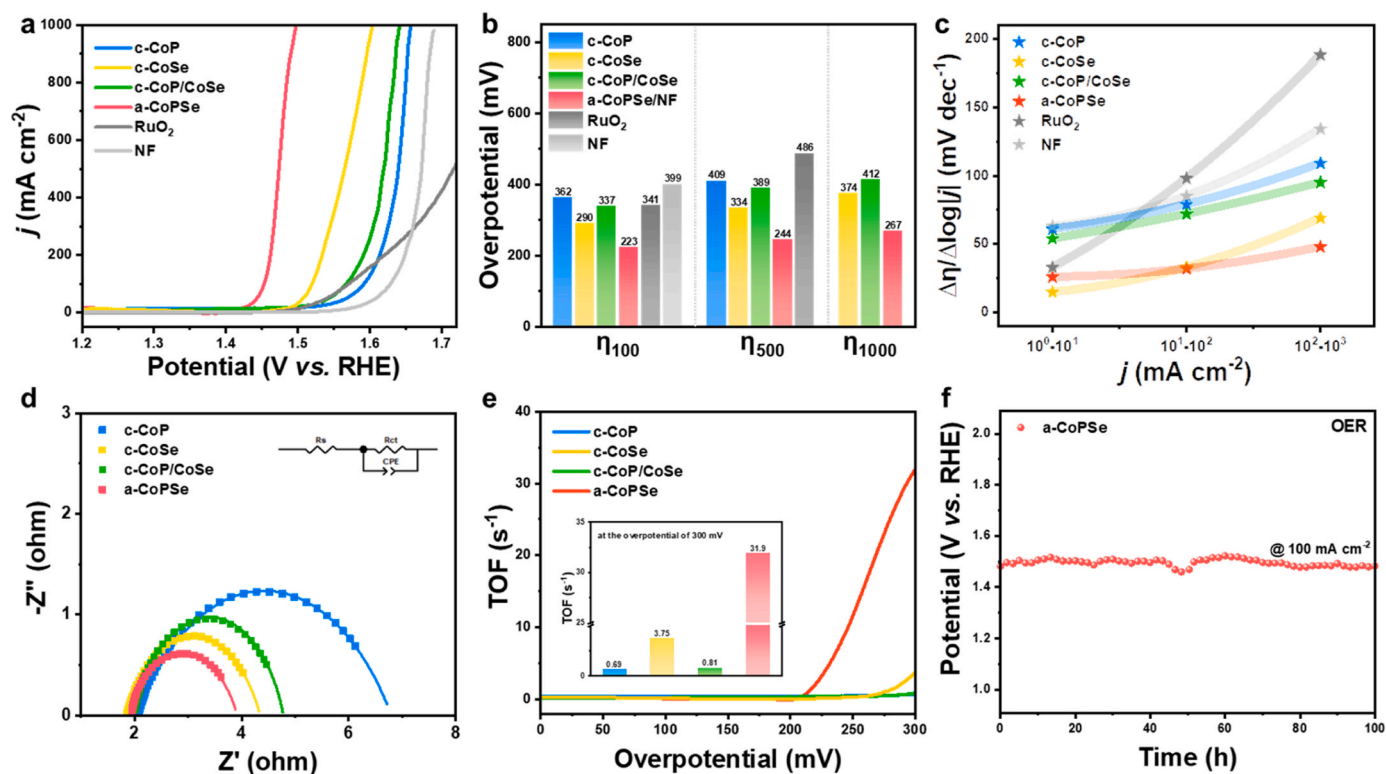

Fig. 4. OER performance in 1.0 M KOH. (a) Polarization curves. (b) The overpotentials at the current density of 100, 500 and 1000 mA cm^{-2}. (c) $\Delta\eta/\Delta\log|j|$ ratios at different current densities. (d) Nyquist plots. (e) TOF values. (f) Chronopotentiometry curve of a-CoPSe.

density, indicating a clear kinetic advantage of the catalysts. It indicates that the a-CoPSe proceeds with faster kinetic during the HER process. In addition, electrochemical impedance spectroscopy (EIS) is also a significant indicator to evaluate the reaction kinetics. The EIS of as-prepared electrodes are shown as the Nyquist plots in Fig. 3d. Specific data are presented in Table S2. It can be observed that a-CoPSe possesses a smaller charge transfer resistance (R_{ct}), facilitating charge transfer during HER. The ECSA is determined by the C_{dl}. The C_{dl} was calculated by cyclic voltammogram (CV) tests at different scanning rates (Fig. S15). As shown in Fig. S16, the C_{dl} value of a-CoPSe (52.7 mF cm^{-2}) is much larger than that of c-CoP (33.3 mF cm^{-2}), c-CoSe (43.2 mF cm^{-2}) and c-CoP/CoSe (48.1 mF cm^{-2}), demonstrating more active sites exposed for a-CoPSe electrode. Likewise, the ECSA of a-CoPSe electrode is optimal (65.9 m^{2}g^{-1}), which contributes to accelerating electrocatalytic reactions and mass transfer (Fig. S16). To assess the intrinsic HER activity quantitatively, the TOF values of catalysts were calculated. In Fig. 3e, the a-CoPSe presents a TOF value of 35.7 s^{-1} at the overpotential of 300 mV, higher than that of c-CoP (17.1 s^{-1}), c-CoSe (9.3 s^{-1}) and c-CoP/CoSe (21.4 s^{-1}) at the same overpotential. Furthermore, the catalytic stability of a-CoPSe electrode is also remarkable. Compared to the initial curve, the LSV curve after 1000 CV cycles only slightly deteriorated (Fig. S19). Moreover, the chronopotentiometry curve and LSV curve after stability testing jointly shows the impressive stability of a-CoPSe electrode (Fig. 3f and S20).

Subsequently, the OER performance of catalysts was determined in the same operating conditions. The commercial RuO$_2$ was included as a benchmark comparison. The OER polarization curves of samples after 95% iR compensation are shown in Fig. 4a. It can be clearly observed that a-CoPSe electrode possesses the most efficient OER activity. The overpotentials of a-CoPSe at the current densities of 100, 500 and 1000 mA cm^{-2} are only 223, 244 and 267 mV, far less than other comparison nanomaterials (Fig. 4b). In Fig. 4c, the Tafel slopes of a-CoPSe are not only small in values, but also grow slowly with increasing current density, suggesting excellent OER kinetic. Meanwhile, a-CoPSe exhibits the smallest R_{ct} than other catalysts, exhibiting excellent kinetics during the OER process (Fig. 4d). The corresponding data are shown in Table S3. Thereafter, TOF values of the prepared electrodes were calculated to evaluate the intrinsic OER activity. As shown in Fig. 4e, the a-CoPSe offers a TOF value of 31.9 s^{-1} at the overpotential of 300 mV, higher than that of c-CoP (0.69 s^{-1}), c-CoSe (3.75 s^{-1}) and c-CoP/CoSe (0.81 s^{-1}) at the same overpotential. Furthermore, the results of multiple CV cycles and chronopotentiometry measurements collectively prove that a-CoPSe presents excellent stability during the OER process (Fig. 4f and S21). The LSV curve of a-CoPSe after long-term stability testing in 1.0 M KOH shows the slightly deteriorated of OER activity (Fig. S22). The above electrochemical evaluation results demonstrate that as-prepared a-CoPSe electrode delivers very promising activity in both HER and OER processes, even outperforming most reported transition metal-based catalysts (Table S3 and S4).

In addition, the effect of electrodeposition time on the morphology and performance of the amorphous cobalt phosphoselenide was also investigated. Maintaining other conditions constant, a-CoPSe-5 min, a-CoPSe-15 min and a-CoPSe-20 min were prepared by adjusting galvanostatic electrodeposition times. SEM images of the prepared catalysts are shown in Fig. S23. With the increase of electrodeposition time, the amorphous CoPSe nanosheets on the surface of nickel foam gradually increase and even accumulate into a block structure. However, it should be noted that increasing time also causes the original loose structure to gradually dense, which is likely to harm the exposure of active sites and electrolyte contact. Moreover, we determined the amorphous CoPSe nanomaterial loading on the surface of the NF substrate after different deposition times and performed a fit to the data (Fig. S24). The fitting results demonstrate that the mass loading is proportional to the electrodeposition time. To verify the above prediction, the electrocatalytic properties of the relevant nanomaterials were studied. The HER polarization curves of samples after 95% iR compensation are shown in

Fig. S25a. As anticipated, the HER activity of the catalyst tends to increase and then decrease during the period of 5–15 min. The initial improvement is attributed to the enhancement of the active sites, and the subsequent decrease is caused by partial overwriting of the active site. When the electrodeposition time increases to 20 min, the HER activity will increase again with sufficient mass loading, but it is not cost-effective in terms of mass activity. A similar regularity also appears in the OER activity analysis. In Fig. S25b, the optimal OER catalytic activity was achieved at 10 min over a deposition time of 5–20 min. At the current density of 500 mA cm^{-2}, the overpotentials of different catalysts for HER and OER were summarized in Fig. S25c. It is evident that an electrodeposition time of 10 min is the most reasonable choice for constructing a bifunctional amorphous CoPSe catalyst. Meantime, the mass activities of a-CoPSe were calculated in Fig. S26. At the overpotential of 250 mV, the prepared a-CoPSe shows outstanding mass activities with 214.2 and 677.4 A g$_{Co}^{-1}$ during HER and OER processes.

3.3. DFT calculations

To deeply elaborate on the excellent HER and OER performances of a-CoPSe, density functional theory (DFT) calculations were performed to investigate the electronic modulation of amorphous cobalt atoms. The computational details are shown in the supplementary information. Firstly, the total density of states (DOS) of c-CoP, c-CoSe and a-CoPSe were depicted in Fig. 5a-c. Compared with the other catalysts, a-CoPSe displayed more DOS near the Fermi level, indicating higher electrical conductivity and faster charge transfer capability [20,48–50]. By resolving the D-band centers of different structures, the adsorption strength of the active sites to the reactant molecules can be evaluated. The D-band centers of a-CoPSe were at − 1.14 eV, which is closer to the Fermi level than that of c-CoP (−1.44 eV) and c-CoSe (−1.20 eV). These results suggest that the electronic structure of a-CoPSe provides enhanced interaction between catalytic sites and activated intermediates [51].

In order to further analyze the catalytic mechanism and understand the relationship between electronic structure and the intrinsic activity of the catalysts, the ΔG of each reaction step was calculated. For the HER that occurs in alkaline electrolytes, the electrocatalysts are always required to adsorb water on the surface and then dissociate the water molecules. Therefore, efficient adsorption and dissociation of water molecules are highly desired for water splitting. As shown in Fig. 5d, the adsorption of water molecules is a thermodynamically favorable process, and a-CoPSe have a lower energy barrier (0.34 eV) to dissociate a water molecule than those of c-CoP (0.50 eV) and c-CoSe (0.81 eV). It is well known that the ΔG_{H*} is an important indicator to predict and evaluate the HER activity of the catalysts. The ΔG_{H*} is closer to the ideal value of 0 eV, which means that the catalyst is more favorable to hydrogen desorption. In Fig. 5e, the ΔG_{H*} of a-CoPSe was calculated to be − 0.31 eV, significantly better than that of c-CoP (0.53 eV) and c-CoSe (−0.69 eV). Fig. S27 shows the calculated OH$^-$ binding energies (OHBEs) of the prepared catalysts. The OHBE value of a-CoPSe is positive, indicating OH$^-$ species produced by water molecules can be rapidly desorbed from amorphous Co sites. The optimized structures of a-CoPSe involved in the whole HER process are shown in Fig. 5f. The water molecule adsorbs to the amorphous Co sites regulated by phosphorus and selenium atoms for dissociation, after which the generated H* transfer to neighboring phosphorus atoms to form hydrogen and OH* species produced by the breaking down of water molecules can be rapidly desorbed from Co sites. The corresponding structures of c-CoP and c-CoSe are displayed in Fig. S28. These DFT calculation results coincide with experimental data, illustrating that the electronic structure of a-CoPSe facilitates water dissociation, H* adsorption and OH* desorption during HER. In alkaline electrolytes, the OER process contains four electron-proton transfers and involves multiple reaction intermediates. The Gibbs free energy diagrams of the prepared catalysts during OER processes are presented in Fig. 5g. Among the four
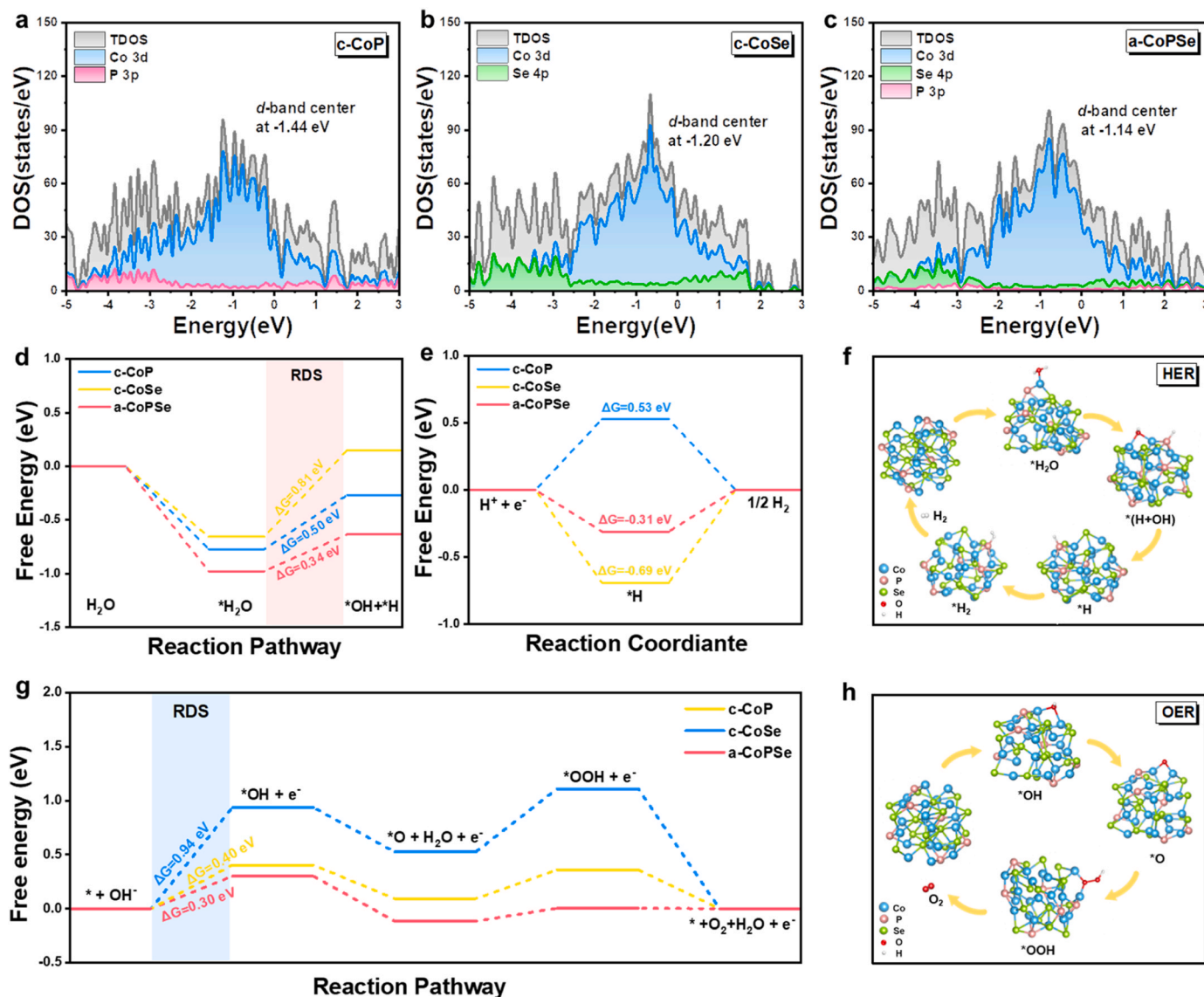
Fig. 5. DFT calculations under alkaline conditions. DOS of (a) c-CoP, (b) c-CoSe and (c) a-CoPSe. (d) Calculated free-energy for HER pathways. (e) Free energy diagrams for H* adsorption. (f) Optimized initial and adsorbed structures of a-CoPSe for HER. (g) Calculated free-energy for OER pathways at the standard potential of 1.23 V. (h) Optimized initial and adsorbed structures of a-CoPSe for OER.

elementary steps, the rate-determining step (RDS) of these catalysts is the formation of OH* . As known, the energy barriers of the RDS are negatively correlated with electrocatalytic activity. Within the standard potential of 1.23 V, the free energy of a-CoPSe (0.30 eV) in the RDS is much reduced than that of c-CoP (0.94 eV) and c-CoSe (−0.40 eV). Moreover, the OOH* generating and oxygen releasing of a-CoPSe were accelerated thanks to lower energy barriers. In addition, the optimized structures of a-CoPSe involved during the OER process were shown in Fig. 5h. The incorporating phosphorus and selenium atoms promote amorphous Co sites as excellent OH acceptors. Then, OH* at the Co site performs a stepwise dehydrogenation and oxygenation process, forming O* and OOH* intermediates and eventually releasing O_2. These jointly indicate that introducing phosphorus and selenium atoms to modulate the electronic structure of the amorphous cobalt sites contributes to the OER kinetics. The corresponding structures of c-CoP and c-CoSe are presented in Fig. S29. To summarize, these DFT analyses demonstrate that the amorphization strategy by introducing phosphorus and selenium atoms enables to promote the HER/OER activity of cobalt-based nanomaterials.

3.4. Performance of overall water splitting

Encouraged by excellent HER and OER performance, the two-electrode overall alkaline water splitting device was assembled with a-CoPSe as both cathode and anode. Similarly, using commercial Pt/C and RuO_2 as cathode and anode, the benchmark two-electrode system was assembled for comparison. As depicted in Fig. 6a, the a-CoPSe‖a-CoPSe couple only needs a cell voltage of 1.89 V to drive the current density of 500 mA cm^{-2}, far superior to Pt/C‖RuO$_2$ couple (2.18 V). Remarkably, this couple can drive 510 mA cm^{-2} at the cell voltage of 1.90 V, which exceeds many reported bifunctional nanomaterials (Fig. 6b). Moreover, the chronopotentiometry curve at 100 mA cm^{-2} manifests good electrocatalytic durability of a-CoPSe‖a-CoPSe couple during constant operation over 100 h (Fig. 6c). The LSV curves of a-CoPSe‖a-CoPSe before and after stability testing were shown in Fig. S30, which further the good stability. Physical characterizations after stability test were carried out. SEM images illustrate that the morphology of a-CoPSe was only slightly changed after HER and OER, proving its excellent morphological stability during the catalytic process (Fig. S31). XPS technology was also employed to investigate the composition and
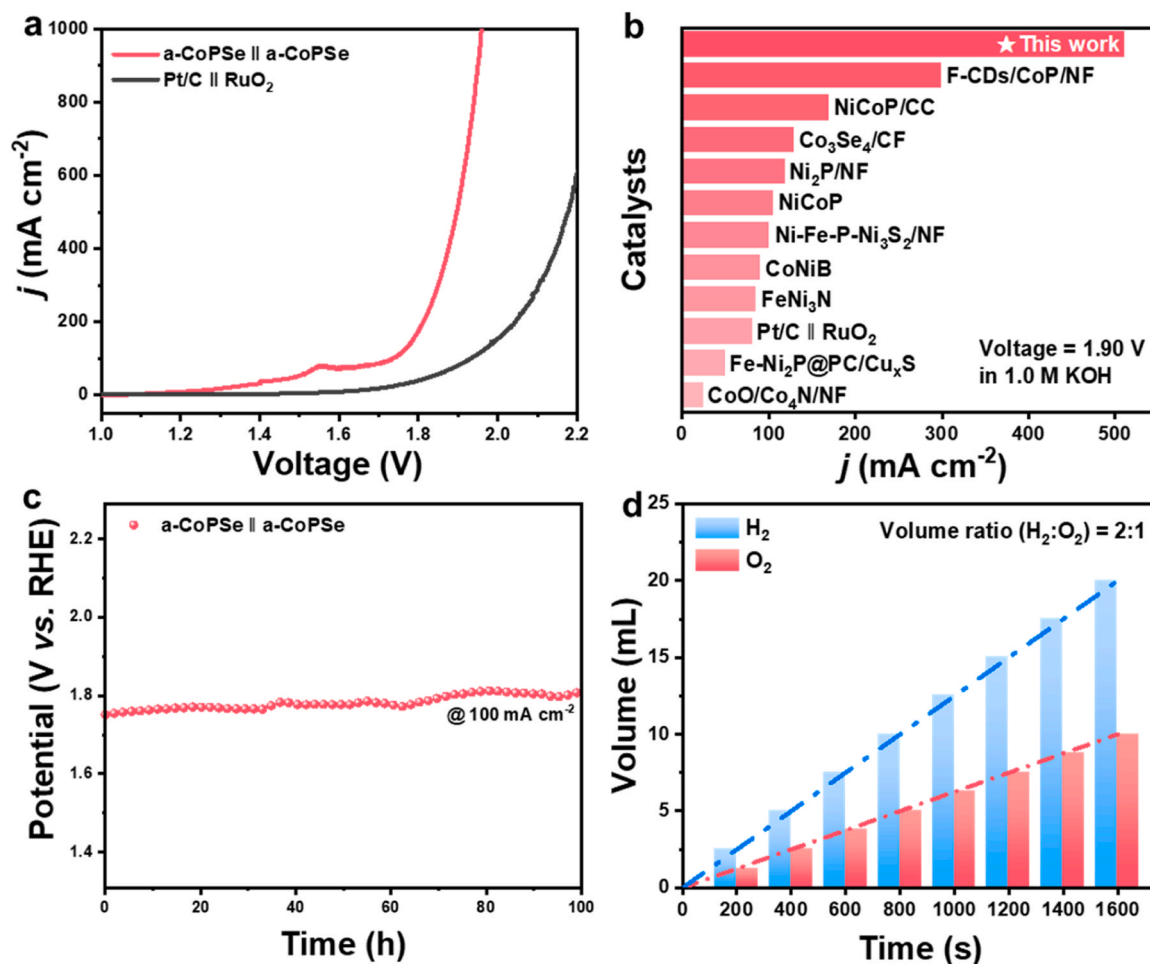
Fig. 6. Overall water splitting performance of a-CoPSe in 1.0 M KOH. (a) LSV curves of two-electrode overall water splitting devices with a-CoPSe ‖ a-CoPSe and Pt/C ‖ RuO$_2$. (b) The current densities of reported catalysts at 1.90 V vs. RHE. (c) Chronopotentiometry curve. (d) The volume of collected H$_2$ and O$_2$ at a series of operating time.

structure of the catalyst after continuous water splitting. In Fig. S32a, the Co 2p XPS spectrum of a-CoPSe after HER is almost the same as the initial a-CoPSe. However, the two dominant peaks of the Co 2p spectrum after OER undergo significant negative shifts, which are associated with Co^{3+} [52]. This change probably results from the in-situ generation of the (oxy)hydroxides, which are considered as the real active species in the OER process [53,54]. After OER, the intensity of P 2p and Se 3d peaks are significantly weaker and shift toward higher binding energy, indicating the dissolution and oxidation of non-metal atoms. After HER, the Se 3d peaks are not visibly shifted and P 2p peaks undergo a slight oxidation. (Fig. S32b-c). As shown in Fig. S33, operando Raman spectra further prove the formation of CoOOH at the applied potential of 1.40 V vs. RHE [55]. The broad Raman peaks of CoOOH illustrate the low crystallinity [56]. Furthermore, the faradic efficiency of the catalysts toward overall water splitting was measured using an H-type electrolytic cell with an anion exchange membrane. The H-type electrolytic cell allows for the effective separation of different gas products from the cathode and anode, thus helping to quantify by drainage method. By recording the volume of the produced gas at a series of operating times, the volume ratio of hydrogen and oxygen is calculated to be 2:1, consistent with the theoretical value (Fig. 6d and S34). It demonstrates the almost 100% faradic efficiency of a-CoPSe toward overall alkaline water splitting. The above performance evaluation collectively shows that a-CoPSe offers promising potential in the field of practical water splitting applications.

4. Conclusion

In summary, we develop the integrated amorphous cobalt phosphoselenide via a simple one-step electrodeposition method to promote efficient alkaline overall water spitting. Phosphorus and selenium atoms with different electronegativities flexibly regulate the electronic structure of the catalyst, thus improving the catalytic activity of integrated catalysts. Detailed electrochemical measurements indicate that as-prepared a-CoPSe delivers favorable HER and OER activity and excellent stability. It only requires the overpotentials of 285 and 244 mV to achieve the current density of 500 mA cm^{-2} during HER and OER, much outperforming commercial catalysts and most reported materials. The a-CoPSe exhibits a desirable ECSA (65.9 m^2 g^{-1}) benefiting from the amorphous structure. It also possesses excellent TOF values (35.7 s^{-1} for HER and 31.9 s^{-1} for OER at the overpotential of 300 mV) owing to the favorable electronic environment. Meanwhile, the mass activities of a-CoPSe are 890.4 A g$_{Co}^{-1}$ for HER at 300 mV and 677.4 A g$_{Co}^{-1}$ for OER at 250 mV, which are comparable to that of commercial Pt/C and RuO$_2$. Moreover, the two-electrode electrolytic cell assembled with a-CoPSe possesses a much lower cell voltage of 1.89 V to deliver 500 mA cm^{-2} than the noble-metal counterpart. The prepared catalyst also presents excellent structural and catalytic stability during the overall water spitting. DFT calculations verify that a-CoPSe offers the optimal DOS, thus enhancing the interaction between active sites and reaction intermediates. Compared to other catalysts, a-CoPSe with the lowest energy barriers of H$_2$O dissociation, H* adsorption, OH* adsorption and

OOH* generation exhibits accelerated HER and OER kinetics. This work innovatively improves the mass activity of non-noble metal catalysts via amorphization and dual anion-mediated strategy, which provides valuable contributions and inspirations in designing and synthesizing efficient catalysts applied in various fields.

CRediT authorship contribution statement

L. Wang and J. Lai supervised the research. J. Lai conceived the research. J. Lai and Y. Shi designed the experiments. Y. Shi performed most of the experiments, data analysis and original draft. S. Zhou, J. Liu and X. Zhang helped with electrochemical measurements. J. Yin performed some physical characterization. T. Zhan, Y. Yang and G. Li helped with data analysis. All authors discussed the results and commented on the manuscript.

Declaration of Competing Interest

The authors declare that they have no known competing financial interests or personal relationships that could have appeared to influence the work reported in this paper.

Data Availability

The authors do not have permission to share data.

Acknowledgment

Appendix A. Supporting information

Supplementary data associated with this article can be found in the online version at doi:10.1016/j.apcatb.2023.123326.

References

[1] X. Lu, L. Yu, X. Lou, Highly crystalline Ni-doped FeP/carbon hollow nanorods as all-pH efficient and durable hydrogen evolving electrocatalysts, Sci. Adv. 5 (2019), eaav6009, https://doi.org/10.1126/sciadv.aav6009.

[2] D. Marin, J. Perryman, M. Hubert, G. Lindquist, L. Chen, A. Aleman, G. Kamat, V. Niemann, M. Stevens, Y. Regmi, S. Boettcher, A. Nielander, T. Jaramillo, Hydrogen production with seawater-resilient bipolar membrane electrolyzers, Joule 7 (2023) 765–781, https://doi.org/10.1016/j.joule.2023.03.005.

[3] L. Wan, M. Pang, J. Le, Z. Xu, H. Zhou, Q. Xu, B. Wang, Oriented intergrowth of the catalyst layer in membrane electrode assembly for alkaline water electrolysis, Nat. Commun. 13 (2022), 7956, https://doi.org/10.1038/s41467-022-35603-9.

[4] J. Chen, M. Aliasgar, F. Zamudio, T. Zhang, Y. Zhao, X. Lian, L. Wen, H. Yang, W. Sun, S. Kozlov, W. Chen, L. Wang, Diversity of platinum-sites at platinum/fullerene interface accelerates alkaline hydrogen evolution, Nat. Commun. 14 (2023), 1711, https://doi.org/10.1038/s41467-023-37404-0.

[5] C. Li, J. Baek, The promise of hydrogen production from alkaline anion exchange membrane electrolyzers, Nano Energy 87 (2021), 106162, https://doi.org/10.1016/j.nanoen.2021.106162.

[6] H. Zhang, G. Shen, X. Liu, B. Ning, C. Shi, L. Pan, X. Zhang, Z. Huang, J. Zou, Self-supporting NiFe LDH-MoSₓ integrated electrode for highly efficient water splitting at the industrial electrolysis conditions, Chin. J. Catal. 42 (2021) 1732–1741, https://doi.org/10.1016/S1872-2067(21)63796-8.

[7] J. Yang, Y. Shen, Y. Sun, J. Xian, Y. Long, G. Li, Ir nanoparticles anchored on metal-organic frameworks for efficient overall water splitting under pH-universal conditions, Angew. Chem. Int. Ed. 62 (2023), e202302220, https://doi.org/10.1002/anie.202302220.

[8] Q. Chen, X. Han, Z. Xu, Q. Chen, Q. Wu, T. Zheng, P. Wang, Z. Wang, J. Wang, H. Li, Z. Xia, J. Hao, Atomic phosphorus induces tunable lattice strain in high

[9] Y. Jiang, H. Liu, Y. Jiang, Y. Mao, W. Shen, M. Li, R. He, Adjustable heterointerface-vacancy enhancement effect in RuO₂@Co₃O₄ electrocatalysts for efficient overall water splitting, Appl. Catal. B Environ. 324 (2023), 122294, https://doi.org/10.1016/j.apcatb.2022.122294.

[10] M. Cong, D. Sun, L. Zhang, X. Ding, In situ assembly of metal-organic framework-derived N-doped carbon/Co/CoP catalysts on carbon paper for water splitting in alkaline electrolytes, Chin. J. Catal. 41 (2020) 242–248, https://doi.org/10.1016/S1872-2067(19)63410-8.

[11] J. Su, J. Zhou, L. Wang, C. Liu, Y. Chen, Synthesis and application of transition metal phosphides as electrocatalyst for water splitting, Sci. Bull. 62 (2017) 633–644, https://doi.org/10.1016/j.scib.2016.12.011.

[12] Y. Zang, D. Lu, K. Wang, B. Li, P. Peng, Y. Lan, S. Zang, A pyrolysis-free Ni/Fe bimetallic electrocatalyst for overall water splitting, Nat. Commun. 14 (2023), 1792, https://doi.org/10.1038/s41467-023-37530-9.

[13] W. Luo, Q. Gao, Z. Ma, X. Ma, Y. Jiang, W. Shen, R. He, W. Su, M. Li, Interface-vacancy synergy of Co(OH)₂/CoN to boost alkaline water splitting, Sci. China Mater. 66 (2023) 2246–2256, https://doi.org/10.1007/s40843-022-2386-3.

[14] Y. Chen, J. Yu, J. Jia, F. Liu, Y. Zhang, G. Xiong, R. Zhang, R. Yang, D. Sun, H. Liu, W. Zhou, Metallic Ni₃Mo₃N porous microrods with abundant catalytic sites as efficient electrocatalyst for large current density and superstability of hydrogen evolution reaction and water splitting, Appl. Catal. B Environ. 272 (2020), 118956, https://doi.org/10.1016/j.apcatb.2020.118956.

[15] Q. Xu, J. Zhang, H. Zhang, L. Zhang, L. Chen, Y. Hu, H. Jiang, C. Li, Atomic heterointerface engineering overcomes the activity limitation of electrocatalysts and promises highly-efficient alkaline water splitting, Energy Environ. Sci. 14 (2021) 5228–5259, https://doi.org/10.1039/D1EE02105B.

[16] K. Wang, Y. Guo, Z. Chen, D. Wu, S. Zhang, B. Yang, J. Zhang, Regulating electronic structure of two-dimensional porous Ni/Ni₃N nanosheets architecture by Co atomic incorporation boosts alkaline water splitting, InfoMat 4 (2022), e12251, https://doi.org/10.1002/inf2.12251.

[17] M. Li, Z. Zhao, Z. Xia, M. Luo, Q. Zhang, Y. Qin, L. Tao, K. Yin, Y. Chao, L. Gu, W. Yang, Y. Yu, G. Lu, S. Guo, Exclusive strain effect boosts overall water splitting in PdCu/Ir core/shell nanocrystals, Angew. Chem. Int. Ed. 60 (2021) 8243–8250, https://doi.org/10.1002/anie.202016199.

[18] S. Zhang, G. Gao, H. Zhu, L. Cai, X. Jiang, S. Lu, F. Duan, W. Dong, Y. Chai, M. Du, In situ interfacial engineering of nickel tungsten carbide Janus structures for highly efficient overall water splitting, Sci. Bull. 65 (2020) 640–650, https://doi.org/10.1016/j.scib.2020.02.003.

[19] J. Lee, H. Jung, Y. Park, N. Kwon, S. Woo, N. Selvam, G. Han, H. Jung, P. Yoo, S. Choi, J. Han, B. Lim, Chemical transformation approach for high-performance ternary NiFeCo metal compound-based water splitting electrodes, Appl. Catal. B Environ. 294 (2021), 120246, https://doi.org/10.1016/j.apcatb.2021.120246.

[20] Y. Sun, W. Sun, L. Chen, A. Meng, G. Li, L. Wang, J. Huang, A. Song, Z. Zhang, Z. Li, Surface reconstruction, doping and vacancy engineering to improve the overall water splitting of CoP nanoarrays, Nano Res. 16 (2023) 228–238, https://doi.org/10.1007/s12274-022-4702-y.

[21] Y. Liu, S. Xu, X. Zheng, Y. Lu, D. Li, D. Jiang, Ru-doping modulated cobalt phosphide nanoarrays as efficient electrocatalyst for hydrogen evolution rection, J. Colloid Interface Sci. 625 (2022) 457–465, https://doi.org/10.1016/j.jcis.2022.06.059.

[22] C. Huang, J. Zhou, D. Duan, Q. Zhou, J. Wang, B. Peng, L. Yu, Y. Yu, Roles of heteroatoms in electrocatalysts for alkaline water splitting: a review focusing on the reaction mechanism, Chin. J. Catal. 43 (2022) 2091–2110, https://doi.org/10.1016/S1872-2067(21)64052-4.

[23] Y. Men, Y. Tan, P. Li, X. Cao, S. Jia, J. Wang, S. Chen, W. Luo, Tailoring the 3d-orbital electron filling degree of metal center to boost alkaline hydrogen evolution electrocatalysis, Appl. Catal. B Environ. 284 (2021), 119718, https://doi.org/10.1016/j.apcatb.2020.119718.

[24] D.T. Tran, H.T. Le, V.H. Hoa, N.H. Kim, J.H. Lee, Dual-coupling ultrasmall iron-Ni₂P into P-doped porous carbon sheets assembled CuₓS nanobrush arrays for overall water splitting, Nano Energy 84 (2021), 105861, https://doi.org/10.1016/j.nanoen.2021.105861.

[25] T. Wu, S. Xu, Z. Zhang, M. Luo, R. Wang, Y. Tang, J. Wang, F. Huang, Bimetal modulation stabilizing a metallic heterostructure for efficient overall water splitting at large current density, Adv. Sci. 9 (2022), 2202750, https://doi.org/10.1002/advs.202202750.

[26] T. Cui, X. Zhai, L. Guo, J. Chi, Y. Zhang, J. Zhu, X. Sun, L. Wang, Controllable synthesis of a self-assembled ultralow Ru, Ni-doped Fe2O3 lily as a bifunctional electrocatalyst for large-current-density alkaline seawater electrolysis, Chin. J. Catal. 43 (2022) 2202–2211, https://doi.org/10.1016/S1872-2067(22)64093-2.

[27] G. Kresse, J. Furthmüller, Efficient iterative schemes for ab initio total-energy calculations using a plane-wave basis set, Phys. Rev. B 54 (1996) 11169–11186, https://doi.org/10.1103/PhysRevB.54.11169.

[28] G. Kresse, J. Furthmüller, Efficiency of ab-initio total energy calculations for metals and semiconductors using a plane-wave basis set, Comput. Mater. Sci. 6 (1996) 15–50, https://doi.org/10.1016/0927-0256(96)00008-0.

[29] S. Grimme, Semiempirical GGA-type density functional constructed with a long-range dispersion correction, J. Comput. Chem. 27 (2006) 1787–1799, https://doi.org/10.1002/jcc.20495.

[30] J. Perdew, K. Burke, M. Ernzerhof, Generalized gradient approximation made simple, Phys. Rev. Lett. 77 (1996) 3865–3868, https://doi.org/10.1103/PhysRevLett.77.3865.

[31] H. Monkhorst, J. Pack, Special points for Brillouin-zone integrations, Phys. Rev. B 13 (1976) 5188–5192, https://doi.org/10.1103/PhysRevB.13.5188.

[32] V. Viswanathan, H.A. Hansen, J. Rossmeisl, J.K. Nørskov, Unifying the 2e⁻ and 4e⁻ reduction of oxygen on metal surfaces, J. Phys. Chem. Lett. 3 (2012) 2948–2951, https://doi.org/10.1021/jz301476w.

[33] H. Su, Y. Gorlin, I. Man, F. Calle-Vallejo, J. Nørskov, T. Jaramillo, J. Rossmeisl, Identifying active surface phases for metal oxide electrocatalysts: a study of manganese oxide bi-functional catalysts for oxygen reduction and water oxidation catalysis, Phys. Chem. Chem. Phys. 14 (2012) 14010–14022, https://doi.org/10.1039/C2CP40841D.

[34] H. Ren, L. Yu, L. Yang, Z.-H. Huang, F. Kang, R. Lv, Efficient electrocatalytic overall water splitting and structural evolution of cobalt iron selenide by one-step electrodeposition, J. Energy Chem. 60 (2021) 194–201, https://doi.org/10.1016/j.jechem.2021.01.002.

[35] X. Cao, D. Jia, D. Li, L. Cui, J. Liu, One-step co-electrodeposition of hierarchical radial NixP nanospheres on Ni foam as highly active flexible electrodes for hydrogen evolution reaction and supercapacitor, Chem. Eng. J. 348 (2018) 310–318, https://doi.org/10.1016/j.cej.2018.04.209.

[36] A. Toghraei, T. Shahrabi, G. Barati Darband, Electrodeposition of self-supported Ni-Mo-P film on Ni foam as an affordable and high-performance electrocatalyst toward hydrogen evolution reaction, Electrochim. Acta 335 (2020), 135643, https://doi.org/10.1016/j.electacta.2020.135643.

[37] Y. Pei, Y. Yang, F. Zhang, P. Dong, R. Baines, Y. Ge, H. Chu, P.M. Ajayan, J. Shen, M. Ye, Controlled electrodeposition synthesis of Co-Ni-P Film as a flexible and inexpensive electrode for efficient overall water splitting, ACS Appl. Mater. Interfaces 9 (2017) 31887–31896, https://doi.org/10.1021/acsami.7b09282.

[38] T. Tan, P. Han, H. Cong, G. Cheng, W. Luo, An amorphous cobalt borate nanosheet-coated cobalt boride hybrid for highly efficient alkaline water oxidation reaction, ACS Sustain. Chem. Eng. 7 (2019) 5620–5625, https://doi.org/10.1021/acssuschemeng.9b00258.

[39] H. Zhang, B. Chen, H. Jiang, X. Duan, Y. Zhu, C. Li, Boosting water oxidation electrocatalysts with surface engineered amorphous cobalt hydroxide nanoflakes, Nanoscale 10 (2018) 12991–12996, https://doi.org/10.1039/C8NR04195D.

[40] Y. Shi, D. Zhang, H. Miao, W. Zhang, X. Wu, Z. Wang, H. Li, t zhan, X. Chen, J. Lai, L. Wang, A simple, rapid and scalable synthesis approach for ultra-small size transition metal selenides with efficient water oxidation performance, J. Mater. Chem. A 9 (2021) 24261–24267, https://doi.org/10.1039/D1TA07644B.

[41] H. Chen, J. Chen, P. Ning, X. Chen, J. Liang, X. Yao, D. Chen, L. Qin, Y. Huang, Z. Wen, 2D heterostructure of amorphous CoFeB coating black phosphorus nanosheets with optimal oxygen intermediate absorption for improved electrocatalytic water oxidation, ACS Nano 15 (2021) 12418–12428, https://doi.org/10.1021/acsnano.1c04715.

[42] M. Cabán-Acevedo, M. Stone, J. Schmidt, J. Thomas, Q. Ding, H. Chang, M. Tsai, J. He, S. Jin, Efficient hydrogen evolution catalysis using ternary pyrite-type cobalt phosphosulphide, Nat. Mater. 14 (2015) 1245–1251, https://doi.org/10.1038/nmat4410.

[43] M. Luo, Z. Cai, C. Wang, Y. Bi, L. Qian, Y. Hao, L. Li, Y. Kuang, Y. Li, X. Lei, Z. Huo, W. Liu, H. Wang, X. Sun, X. Duan, Phosphorus oxoanion-intercalated layered double hydroxides for high-performance oxygen evolution, Nano Res. 10 (2017) 1732–1739, https://doi.org/10.1007/s12274-017-1437-2.

[44] N. Chen, Y. Du, G. Zhang, W. Lu, F. Cao, Amorphous nickel sulfoselenide for efficient electrochemical urea-assisted hydrogen production in alkaline media, Nano Energy 81 (2021), 105605, https://doi.org/10.1016/j.nanoen.2020.105605.

[45] D. Li, M. Zha, L. Feng, G. Hu, C. Hu, X. Wu, X. Wang, Increased crystallinity of RuSe₂/carbon nanotubes for enhanced electrochemical hydrogen generation performance, Nanoscale 14 (2022) 790–796, https://doi.org/10.1039/D1NR07254D.

[46] N. Nie, D. Zhang, Z. Wang, W. Yu, S. Ge, J. Xiong, Y. Gu, B. Yang, J. Lai, L. Wang, Stable PtNb-Nb₂O₅ heterostructure clusters @CC for high-current-density neutral seawater hydrogen evolution, Appl. Catal. B Environ. 318 (2022), 121808, https://doi.org/10.1016/j.apcatb.2022.121808.

[47] Q. Yu, Z. Zhang, S. Qiu, Y. Luo, Z. Liu, F. Yang, H. Liu, S. Ge, X. Zou, B. Ding, W. Ren, H.-M. Cheng, C. Sun, B. Liu, A Ta-TaS₂ monolith catalyst with robust and metallic interface for superior hydrogen evolution, Nat. Commun. 12 (2021), 6051, https://doi.org/10.1038/s41467-021-26315-7.

[48] X. Shu, M. Yang, M. Liu, H. Wang, J. Zhang, In-situ formation of cobalt phosphide nanoparticles confined in three-dimensional porous carbon for high-performing zinc-air battery and water splitting, Chin. J. Catal. 43 (2022) 3107–3115, https://doi.org/10.1016/S1872-2067(21)64047-0.

[49] L. Zhai, X. She, L. Zhuang, Y. Li, R. Ding, X. Guo, Y. Zhang, Y. Zhu, K. Xu, H.J. Fan, S.P. Lau, Modulating built-in electric field via variable oxygen affinity for robust hydrogen evolution reaction in neutral media, Angew. Chem. Int. Ed. 61 (2022), e202116057, https://doi.org/10.1002/anie.202116057.

[50] L. Zeng, Z. Zhao, F. Lv, Z. Xia, S.-Y. Lu, J. Li, K. Sun, K. Wang, Y. Sun, Q. Huang, Y. Chen, Q. Zhang, L. Gu, G. Lu, S. Guo, Anti-dissolution Pt single site with Pt(OH)(O₃)/Co(P) coordination for efficient alkaline water splitting electrolyzer, Nat. Commun. 13 (2022), 3822, https://doi.org/10.1038/s41467-022-31406-0.

[51] J. Kwon, S. Sun, S. Choi, K. Lee, S. Jo, K. Park, Y. Kim, H. Park, H. Park, J. Jang, H. Han, U. Paik, T. Song, Tailored electronic structure of Ir in high entropy alloy for highly active and durable bi-functional electrocatalyst for water splitting under acidic environment, Adv. Mater. (2023), 2300091, https://doi.org/10.1002/adma.202300091.

[52] P. Menezes, C. Panda, C. Walter, M. Schwarze, M. Driess, A cobalt-based amorphous bifunctional electrocatalysts for water-splitting evolved from a single-source lazulite cobalt phosphate, Adv. Funct. Mater. 29 (2019), 1808632, https://doi.org/10.1002/adfm.201808632.

[53] Q. Qian, Y. Li, Y. Liu, G. Zhang, General anion-exchange reaction derived amorphous mixed-metal oxides hollow nanoprisms for highly efficient water oxidation electrocatalysis, Appl. Catal. B Environ. 266 (2020), 118642, https://doi.org/10.1016/j.apcatb.2020.118642.

[54] Q. Xie, D. Ren, L. Bai, R. Ge, W. Zhou, L. Bai, W. Xie, J. Wang, M. Grätzel, J. Luo, Investigation of nickel iron layered double hydroxide for water oxidation in different pH electrolytes, Chin. J. Catal. 44 (2023) 127–138, https://doi.org/10.1016/S1872-2067(22)64190-1.

[55] W. Peng, A. Deshmukh, N. Chen, Z. Lv, S. Zhao, J. Li, B. Yan, X. Gao, L. Shang, Y. Gong, L. Wu, M. Chen, T. Zhang, H. Gou, Deciphering the dynamic structure evolution of Fe- and Ni-codoped CoS₂ for enhanced water oxidation, ACS Catal. 12 (2022) 3743–3751, https://doi.org/10.1021/acscatal.2c00328.

[56] L. Cao, C. Hu, H. Li, H. Huang, L. Ding, J. Zhang, J. Wu, Z. Du, C. He, X. Chen, Molecule-enhanced electrocatalysis of sustainable oxygen evolution using organoselenium functionalized metal-organic nanosheets, J. Am. Chem. Soc. 145 (2023) 1144–1154, https://doi.org/10.1021/jacs.2c10823.